Comparing SAR based short time-lag cross-correlation and Doppler derived sea ice drift velocities

Thomas Kræmer, Harald Johnsen, Camilla Brekke, Geir Engen

Abstract—This paper shows initial results from estimating Doppler radial surface velocities over Arctic sea ice using the Sentinel-1A satellite. Our study presents the first quantitative comparison between ice drift derived from the Doppler-shifts and drift derived using time series methods over comparable time scales. We compare the Doppler-derived ice velocities to global positioning system tracks from a drifting ice station as well as vector fields derived using traditional cross-correlation between a pair of Sentinel-1A and Radarsat-2 images with a time lag of only 25 minutes. A strategy is provided for precise calibration of the Doppler values in the context of the the Sentinel-1A level-2 ocean radial surface velocity product. When comparing the two methods, root mean squared errors (RMSEs) of 7 cm/s were found for the EW4 and EW5 swaths while the highest RMSE of 32 cm/s was obtained for the EW1 swath. Though the agreement is not perfect, our experiment demonstrates that the Doppler technique is capable of measuring a signal from the ice if the ice is fast moving. However, for typical ice speeds, the uncertainties quickly grow beyond the speeds we are trying to measure. Finally, we show how the application of an antenna pattern correction reduces a bias in the estimated Doppler offsets.

I. INTRODUCTION

With the launch of the Sentinel-1 synthetic aperture radar (SAR) satellites by the European space agency (ESA), new possibilities have emerged for monitoring sea ice motion from space. Through precise estimates of the azimuth (along-track) center frequency or *Doppler centroid* it is possible to obtain a near-instantaneous measurement of the motion of surface scatterers parallel to the pointing direction of the radar antenna. Following the Sentinel-1 level-2 ocean (OCN) product naming convention this line-of-sight (LOS) speed is referred to as a radial surface velocity (RVL) [1]. Doppler-derived radial surface velocities were originally studied in the context of ocean wind and surface current retrieval [2] and later demonstrated over sea ice [3], [4] using data from the advanced synthetic aperture radar (ASAR) instrument on-board the Envisat satellite with encouraging results. The ASAR instrument was not designed with this product in mind, however, and results using stripmap data were degraded by antenna gain problems [4], [5]. In contrast, the Sentinel satellites are constructed to provide very fine control over the antenna, orbit and attitude enabling very high measurement precision.

Ice buoys with high time resolution are the most natural source of data for calibration and validation of radial surface velocities over ice, but the spatial coverage of drifting ice buoys is low as they only provide point measurements. An attractive alternative is to use drift fields derived from frequently available satellite data, where a single SAR scene may cover a swath width in the order of 400–500 km. Two-dimensional ice drift fields are regularly estimated by cross-correlating similar image patterns between pairs of satellite images [6], [7]. A problem with comparing Doppler measurements derived from a single image to cross-correlation (CC) drift vectors derived from a pair of images is that the time separation between scenes can be large (traditionally 1–4 days). Over such time scales, the motion of the ice may be highly non-linear, which prevents a direct quantitive comparison between the two methods [3], [4]. However, due to the increased number of SAR missions orbiting the Earth, we are now at a point where images from multiple satellites can be used together to reduce the time separation between acquisitions to minutes and hours rather than days. This takes us closer to a valid assumption of linear drift between the scenes.

In this paper we estimate the 2-D ice displacement field between a pair of scenes from the Radarsat-2 (RS2) and Sentinel-1A (S1A) satellites with a time spacing of only 25 minutes. We use global positioning system (GPS) tracks from a drifting ice station to check that the ice movement was approximately linear between scenes. The derived CC drift field is then projected onto the antenna LOS and compared with the Doppler RVL drift showing good agreement. We present the S1A RVL product in the context of S1A extra wide swath (EW) mode data, but the algorithm is general and can be applied to any appropriately prepared SAR data (see section III-A for details).

The paper is organized as follows. We first introduce the data selected for the experiments in section II. Section III provides the theoretical background on Doppler frequency estimation from S1A data. Section IV details the cross-correlation algorithm. Results obtained using the two methods are then compared in Section V. Section VI summarizes our findings and provides recommendations for futures studies of RVL for sea ice drift measurements.

II. DATASET

For our experiment we used three sources of ice drift information; GPS positions from a drifting ice station, Doppler derived velocities and cross-correlation displacement measurements. The following gives a brief overview of the dataset.

1) Drifting ice station: In the first half of 2015 the Norwegian Polar Institute (NPI) conducted the Norwegian Young Sea Ice Cruise (N-ICE) whose objective was to increase

Table I: Synthetic aperture radar data used in the experiment

Scene	Sensor	Sensing time [UTC]	Mode	Polarization	Pass direction	Angle of incidence	Nominal looks (Ra x Az)
S1	SENTINEL-1A	2015-03-16 06:05:34	Extra Wide	HH / HV	Descending	19–47°	6 x 2
R1	RADARSAT-2	2015-03-16 06:30:13	ScanSAR Wide	HH / HV	Descending	20–49°	4 x 2
S2	SENTINEL-1A	2015-12-27 10:03:58	Extra Wide	HH / HV	Ascending	19–47°	6 x 2
S3	SENTINEL-1A	2016-01-12 09:55:46	Extra Wide	VV / VH	Descending	19–47°	6 x 2

understanding of the effects of decreasing ice thickness on ice dynamics, energy fluxes and associated local and global climate variables [8]. In late December 2014 the research vessel *Lance* was frozen into an ice floe North of Svalbard to become an ice station passively flowing with the drifting sea ice towards Fram Strait. When the floe broke up or the ship exited the ice the ship moved back into the ice to freeze into another ice floe. The ship continually logged its GPS position with 10 s intervals which we use to check displacement fields derived using CC.

2) Cross-correlation drift: Two-dimensional ice drift vector fields are regularly estimated from pairs of remote sensing images by cross-correlating image patches (technical details given in section IV). For this purpose, operational services normally prefer spaceborne sensors with wide geographical coverage [7]. Traditionally passive microwave instruments have provided rapid revisit times and wide coverage, but with poor resolution in the order of several kilometers. SAR sensors provide a good compromise between wide coverage and high resolution by electronic steering of the antenna in elevation, which periodically illuminates a set of swaths. For RS2 this normally means the ScanSAR Wide (SCW) mode which covers an area of ∼500 km x 500 km with a square ground range pixel spacing of 50 m and a resolution of ∼100 m in each dimension [9]. This mode uses four beams which cover incidence angles ranging from 20 to 49 degrees. For S1A, the EW medium resolution product covers an area of ∼400 km x 400 km with a square pixel spacing of 40 m and a resolution of ∼90 m in each dimension [1]. EW mode images are acquired using five beams (EW1–EW5) with incidence angles in the range 19–47 degrees. In contrast with the ScanSAR mode used on RS2, the S1A EW product implements the terrain observation by progressive scans (TOPS) mode which electronically sweeps the antenna in azimuth in addition to stepping in elevation.

From archives of RS2 and S1A scenes we selected data based on the following requirements: A spatial overlap of at least 40% between images was desired to obtain a reasonably large 2-D drift field using CC. At the same time we wanted the time spacing between images to be as small as possible, while still allowing the ice to be displaced sufficiently to be measured by pattern matching. Furthermore, the search was limited to image pairs where the ship was located within both scenes which allows comparison with GPS positions. Because sea ice drift speeds are small compared to surface wind speeds we also wanted to have reasonably high drift speeds to increase chances of having detectable Doppler shifts. Therefore, we also included the ice speed (estimated from the ship's GPS) in

the search. The image pair (S1, R1) in Table I stood out as an excellent candidate. The other scenes are used for calibration investigations.

3) Doppler-derived drift: The Doppler estimation algorithm requires a full-bandwidth processed single-look complex (SLC) image as input. This is not a standard S1A product and we therefore require that the raw unfocused (Level-0) data is available so a custom SLC can be created without using window functions, thereby retaining the full bandwidth of the data. Raw data was not available for RS2 and hence Doppler-derived velocities were calculated for S1A scenes only. We therefore use Doppler anomalies from homogeneous parts of S2 to calibrate the Doppler anomalies in S1.

All the scenes had two polarization channels; horizontal transmit/horizontal receive (HH) and horizontal transmit/vertical receive (HV). In our experiments we have focused on the HH polarization only. This has long been the preferred channel for many sea ice applications, however the algorithms are not limited to use a particular polarization. For CC drift estimation it has been shown that use of both channels may be beneficial [7]. Although the Doppler estimation algorithm presented in section III does not assume a particular polarization, it should be noted that the signal-to-noise ratio (SNR) over ice and water is often lower compared to HH which will lead to larger uncertainties in the RVL estimates.

III. DOPPLER-DERIVED RADIAL SURFACE VELOCITY MEASUREMENT AND CALIBRATION

The SAR imaging process can be formulated as a convolution of the transmitted signal modulation with the ground reflectivity, weighted by the antenna directivity pattern [10]. High resolution is achieved by pulse compression in both the across track and along track direction by proper modeling and matched filtering of the target phase history $\phi = -2kR$ [rad] where R is the sensor–target range, $k = 2\pi/\lambda$ is the wavenumber and λ is the wavelength. As the satellite moves, the relative range between the antenna and the ground changes at a rate $\dot{R}$, introducing Doppler shifts in the signal. The angular *Doppler centroid* in [rad/s]

$$\varpi_{dc} = -2k\dot{R}(\tau_0) = -2k\boldsymbol{v_{rel}} \cdot \hat{\boldsymbol{r}} \qquad (1)$$

is the frequency offset corresponding to the time τ_0 when the target is in the beam center. Here, $\boldsymbol{v_{rel}} = \boldsymbol{v_t} - \boldsymbol{v_s}$ is the relative velocity between the sensor ($\boldsymbol{v_s}$) and target ($\boldsymbol{v_t}$) and $\hat{\boldsymbol{r}}$ is a unit vector pointing from the sensor to the target. Note that only the projection of the relative velocity onto the LOS matters, and hence any along track target motion is not observable using Doppler measurements.

Angular frequencies in [rad/s] are related to their linear counterpart in Hz by a factor 2π. The pulsed nature of the SAR system limits the observable ϖ_{dc} values to the baseband region $[-\varpi_{prf}/2, \varpi_{prf}/2]$, where ϖ_{prf} is the angular pulse repetition frequency (PRF). In general the Doppler centroid, ϖ'_{dc}, may be expressed as $\varpi'_{dc} = \varpi_{dc} + M\varpi_{prf}$ where ϖ_{dc} is the *fractional Doppler centroid* and M is an integer referred to as the *Doppler ambiguity* [10]. It is common for SAR satellites to follow a yaw-steering law which adjusts the antenna pointing direction as a function of latitude to provide $M = 0$. In this paper we therefore only consider the fractional part ($\varpi'_{dc} = \varpi_{dc}$), but in general the ambiguity would have to be estimated as well. Estimation of both ϖ_{dc} and M is covered in standard texts on SAR such as [10, ch. 12]).

At any position we can model the measured Doppler centroid as a linear combination of (i) Doppler shifts due to the relative sensor–target motion as predicted by eq. (1) and (ii) Doppler shifts due to antenna effects,

$$\varpi_{dc} \approx \varpi_{geom} + \varpi_{phys} + \varpi_{em} \qquad (2)$$

where ϖ_{geom} is the contribution due the relative motion between the satellite and a *stationary target* on the surface of the rotating Earth, ϖ_{phys} is the geophysical Doppler shift due to the LOS motion of surface scatterers relative to the rotating Earth and ϖ_{em} is a bias introduced by the antenna electronic mispointing [11].

1) Geometric Doppler, ϖ_{geom}: The geometric contribution can be calculated by solving the range–Doppler equations taking into account the sensor attitude. This is explained in great detail in standard textbooks on SAR (see e.g. [10, chap. 12]). S1A uses total zero-Doppler steering which combines yaw-steering with an additional pitch-steering to provide a nominally zero geometric Doppler ($\varpi_{geom} \approx 0$) across the entire swath [12].

2) Electronic mispointing, ϖ_{em}: The most commonly used antennas for spaceborne SARs are phased array systems which have the ability to electronically steer the beam in both azimuth and elevation as well as the freedom to shape the antenna pattern by varying the amplitude and phase of each transmit/receive module (TRM). Over time, the characteristics of the TRMs change due to drift in the electronics or physical damage to the antenna. For a given elevation angle, these deviations may cause the maximum gain to occur at an azimuth angle slightly offset from the nominal pointing angle which introduces an unintentional squint. The effect, known as *electronic mispointing*, contributes to an offset ϖ_{em} which is a function of elevation angle only. If the embedded row patterns, error matrix and excitation coefficients are available, the full antenna pattern can be simulated and the mispointing estimated directly using the antenna model presented in [13]. However, publicly available auxiliary calibration files for S1A (referred to as AUX_CAL in ESA documentation [14]) only provide two slices of the antenna and this dyadic approximation hence does not capture the range variation of the mispointing. Alternatively ϖ_{em} can be estimated from data over stationary areas of homogeneous backscatter. This is discussed further in section V where mispointing profiles

predicted by the antenna model are compared with estimates from rainforest data.

3) Geophysical Doppler, ϖ_{phys}: By explaining away contributions from the motion of the Earth and antenna effects we can invert eq. (2) to obtain the parameter of interest, ϖ_{phys}; the Doppler shift due to the geophysical motion of scatterers on the surface:

$$\varpi_{phys} \approx \varpi_{dc} - \varpi_{geom} - \varpi_{em}. \qquad (3)$$

Referring to eqs. (1) and (3), the target LOS speed u_r can be calculated as

$$u_r = -\frac{\varpi_{phys}}{2k}. \qquad (4)$$

In [2], Chapron et al. interpreted the target speed u_r using a simple geometrical model,

$$u_r = \frac{\langle (u_g \sin\theta_i - u_v \cos\theta_i)\sigma(\theta'_i) \rangle}{\langle \sigma(\theta'_i) \rangle} \qquad (5)$$

where $\langle \cdot \rangle$ denotes ensemble averaging over the local incidence angles θ'_i, θ_i is the angle of incidence at the center of the estimation cell, u_g is the target speed tangential to the surface, u_v is the target speed normal to the surface, and σ is the signal intensity. Following [3], assuming homogeneous backscatter and no vertical motion in the central ice pack ($u_v = 0$), we can approximate the ground range surface velocity u_g as

$$u_g \approx \frac{u_r}{\sin\theta_i}. \qquad (6)$$

This is of course not always a good assumption, and we discuss this further in section V. The rest of this section details the baseband Doppler centroid estimation algorithm.

A. Preprocessing

SLC data for the EW mode is not a standard product delivered by ESA. We therefore take the unfocused raw data (Level-0) as our starting point and focus each burst to an SLC using an ω–K algorithm adapted for TOPS mode data [15]. No window functions are applied during focusing, thereby retaining the full bandwidth of the data.

Let $I^{(m)}(\boldsymbol{t})$ denote the m-th complex-valued SLC burst where $\boldsymbol{t} = (t, \tau)$ denotes range time (t) and azimuth time (τ). While aquiring each burst, the TOPS mode sweeps the antenna in azimuth, changing the beam center angle at a rate k_ψ [rad/s]. The one-to-one relationship between the beam center angle and the Doppler centroid means that a linear sweep of the antenna introduces an approximately linear change in the Doppler centroid at a rate k_a [Hz/s] given by

$$k_a \approx -\frac{2v_s}{\lambda}k_\psi$$

where v_s is the platform speed. This phase ramp in the SLC data must be removed before traditional Doppler estimators can be used [16]. A deramped SLC burst, $I_d^{(m)}(\boldsymbol{t})$, can be produced by multiplying the burst with a chirp

$$I_d^{(m)}(\boldsymbol{t}) = I^{(m)}(\boldsymbol{t})e^{-jk_t(\tau - \tau_c^{(m)})^2} \qquad (7)$$

where $j = \sqrt{-1}$, $k_t = k_a/\alpha$ and $\tau_c^{(m)}$ denotes the azimuth time of the m-th burst center.

As described in [16], the range-dependent factor α given by

$$\alpha = 1 + \frac{k_a}{|k_r|} \qquad (8)$$

can be interpreted as an antenna scaling factor relating a physical antenna operating in TOPS mode to a mathematically equivalent scaled antenna operating in stripmap mode. Here,

$$k_r \approx -\frac{2v_{eff}^2}{\lambda r_0} \qquad (9)$$

is the range-dependent Doppler rate, $v_{eff} = \sqrt{v_s v_g}$ is the range-varying *effective* sensor speed (see e.g. [10, p. 127]), v_g is the gound speed of the antenna footprint, and r_0 is the range at the time of closest approach.

After deramping the bursts are merged onto a common grid to obtain a connected SLC image $I(\boldsymbol{t})$ per swath using the procedure outlined in appendix A. From each swath, the Doppler centroid is estimated blockwise on a regular grid where the block size is 298×228 pixels in range and azimuth direction ($\sim 4.2 \times 9.5$ km), respectively, and the step size is 25% of block side lengths. The Doppler estimation procedure is described in the following section.

B. Doppler estimation and side-band correction

Doppler centroid estimators exploit the observation that the azimuth power spectrum of the data, $P(\varpi; \boldsymbol{t})$, is related to the two-way azimuth antenna directivity pattern $D(\varpi)$, where ϖ denotes the azimuth-direction (Doppler) frequency [17]. The observed power spectrum estimated from a block of data centered at time $\boldsymbol{t}$ is given by

$$P(\varpi; \boldsymbol{t}) = \int dt' \left| \int d\tau' I(\boldsymbol{t}') h(\boldsymbol{t}' - \boldsymbol{t}) e^{-j\varpi\tau'} \right|^2 \qquad (10)$$

where $h(\boldsymbol{t}') = h_r(t') h_a(\tau')$ is a dyadically constructed window function satisfying $\int h_r(t') dt' = \int h_a(\tau') d\tau' = 1$ and the integration is over a data block of size (B_r, B_a) in range and azimuth, respectively. Estimation of the Doppler centroid therefore amounts to finding the Doppler frequency ϖ_{dc} that provides the best fit between the observed power spectrum and a model spectrum based on the expected antenna pattern described below.

The antenna pattern extends well beyond the PRF which means that energy in the side bands, i.e., signal components outside the main band $[-\varpi_{prf}/2, \varpi_{prf}/2]$ will fold (alias) into the main band resulting in azimuth ambiguities (also referred to as *ghost images*) [10]. This is equivalent to energy from neighboring geographical areas influencing the spectrum of the estimation area. The degree of aliasing depends on the PRF location relative to the antenna pattern, but typically there is only significant energy coming from the first side band. In the case of high SNR and homogeneous data, this aliasing process results in a power spectrum that is well modeled by a raised cosine [18]. This is the motivation for time-domain estimators which exploit the Fourier pair relationship between the autocorrelation function and the power spectrum (Wiener–Khinchin theorem) [18]. In inhomogeneous areas, backscatter registered through the side bands of the antenna may contribute

significantly to the total power. This typically happens close to shore, where the beam center covers the ocean which may have low backscatter, while the side bands cover neighboring mountain areas with high backscatter. A consequence of the pulsed operation of the SAR system is that the spectrum is periodic. For a stripmap system, this periodicity follows the raw data PRF, ϖ_{prf}, but for TOPS we need to take into account the antenna scaling factor α making the data periodic with a separation of $\varpi_\Delta = \varpi_{prf}/\alpha$.

Building on work by Madsen [18] and Bamler [19], Engen and Johnsen [20] therefore modeled the expected power spectrum $P(\varpi; \boldsymbol{t})$ as the sum of the frequency folded antenna pattern weigted by the average intensity $\sigma(\boldsymbol{t}_l)$ within each side band and a white noise component $b(\boldsymbol{t})$ capturing the thermal and quantization noise.

By introducing the normalized azimuth frequency $\eta = \varpi/\varpi_\Delta$, the model for the azimuth spectrum can be expressed as

$$P(\eta; \boldsymbol{t}) = W(\eta - \varsigma_0) \left[\sum_l \sigma(\boldsymbol{t}_l) D_l(\eta - \varsigma(\boldsymbol{t}_l)) + b(\boldsymbol{t}) \right] \qquad (11)$$

where

$$D_l(\eta) = D((\eta + l)\varpi_{prf}) \qquad (12)$$

is the two-way antenna gain pattern of the l-th side band, W is a window covering the critical bandwidth ϖ_Δ, centered on ς_0, the normalized Doppler centroid used during focusing and ς is the normalized Doppler centroid we wish to estimate. The time $\boldsymbol{t}_l = \boldsymbol{t} + \Delta \boldsymbol{t}_l$ is the position of the l-th ghost image where the range component of $\Delta \boldsymbol{t}_l$ is the range migration and the azimuth component is $l \cdot f_{prf}/k_r$ ($\Delta \boldsymbol{t}_l = 0$ for $l = 0$).

The corresponding autocorrelation coefficients (index by n) given by

$$p_n(\boldsymbol{t}) = \int d\eta P(\eta; \boldsymbol{t}) e^{j2\pi n\eta} \qquad (13)$$

are then

$$p_n(\boldsymbol{t}) = \sum_l f_n(\boldsymbol{t}_l) d_n(l + \Delta l(\boldsymbol{t}_l)) + b(\boldsymbol{t})\delta_n \qquad (14)$$

where $f_n(\boldsymbol{t}) = \sigma(\boldsymbol{t}) e^{-j2\pi n\varsigma}(\boldsymbol{t})$ are the side-band corrected autocorrelation coefficients, $\Delta l(\boldsymbol{t}) = \varsigma_0 - \varsigma(\boldsymbol{t})$ is the offset between the Doppler centroid used during focusing and the true Doppler centroid, δ is the Kroenecker delta function ($\delta_0 = 1$, $\delta_{n \neq 0} = 0$) and

$$d_n(\lambda) = \int d\eta D(\eta) W(\eta - \lambda) e^{j2\pi n\eta}. \qquad (15)$$

The coefficients f_1 and f_0 are of special interest as the first coefficient provides an estimate of the average signal intensity and the true Doppler centroid, and the zeroth order coefficient can be used to estimate the additive noise level. We can invert eq. (14) solving for f_1 by introducing

$$\epsilon(\boldsymbol{t}) = \sum_l f_1(\boldsymbol{t}_l)(d_1(l + \Delta l(\boldsymbol{t}_l)) - d_1(l)) \qquad (16)$$

expressing the first correlation coefficient as

$$p_1(\boldsymbol{t}) = \sum_l f_1(\boldsymbol{t}_l) d_1(l) + \epsilon(\boldsymbol{t}) \qquad (17)$$
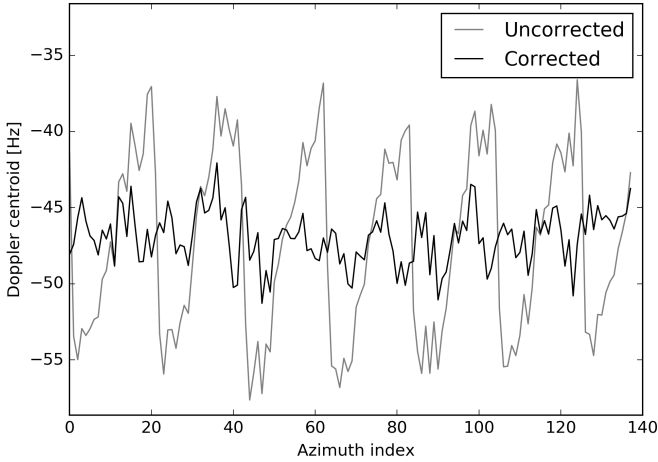
Figure 1: Effect of antenna element pattern (AEP) correction of raw data on Doppler centroids estimated from the EW3 swath of the S3 rainforest scene. If the correction is not applied, the estimated Doppler centroids contain an approximately linear trend in azimuth within each burst.

and exploiting the Fourier shift property

$$\tilde{p}_1(\boldsymbol{\omega}) = \sum_l \tilde{f}_1(\boldsymbol{\omega}) e^{-j\boldsymbol{\omega}\cdot\Delta\boldsymbol{t}_l} d_1(l) + \tilde{\epsilon}(\boldsymbol{\omega}) \qquad (18)$$

from which we can obtain

$$f_1(\boldsymbol{t}) = \mathcal{F}^{-1}\left\{\frac{\tilde{p}_1(\boldsymbol{\omega}) - \tilde{\epsilon}(\boldsymbol{\omega})}{\sum_l d_1(l) e^{-j\boldsymbol{\omega}\cdot\Delta\boldsymbol{t}_l}}\right\} \qquad (19)$$

Here, $\tilde{x}(\boldsymbol{\omega}) = \mathcal{F}\{x(\boldsymbol{t})\}$ denotes the Fourier transform of $x(\boldsymbol{t})$ with corresponding inverse transform $x(\boldsymbol{t}) = \mathcal{F}^{-1}\{\tilde{x}(\boldsymbol{\omega})\}$ and the implicit dependency on f_1 through ϵ can be solved by fix point iteration of eq. (19) starting with the assumption that $\varsigma = \varsigma_0$ ($\epsilon = 0$). The Doppler centroid is then $\varpi_{dc} = \varsigma\varpi_{prf}$.

If the described Doppler estimation algorithm is applied as stated to the SLC data a trend in the Doppler can be observed within each burst (see fig. 1). This can be explained by the elevation direction antenna element pattern (AEP) envelope which weighs the total phased array beam pattern and biasing the beam center slightly. The effect can be mitigated by either calculating the resulting Doppler offset and including another correction term in eq. (5) or by dividing the raw data by the element pattern to flatten the data before Doppler estimation. Antenna pattern profiles are provided in the AUX_CAL auxiliary files made available at https://qc.sentinel1.eo.esa.int/. Both options provide trade-offs. On the one hand, post-processing the estimated Doppler shifts is still sensitive to the small radiometric discontinuity at burst overlaps which can introduce a scalloping pattern with significant harmonics in the estimated Doppler values. On the other hand, applying a gain correction to the data will color the noise and is therefore strictly not in agreement with the proposed model which assumes white noise. However, the gain correction is very small and experiments where both methods were tested with rain forest data showed that the gain correction method gave similar results to the Doppler post-processing method, while providing cleaner estimates in burst overlap zones. We therefore recommend the gain correction method. Uncertainties related to calibration of the Doppler offsets are further discussed in section V.

IV. Cross-correlation drift estimation

Motion estimation algorithms are often categorized into pixel based and feature based algorithms. Pixel based algorithms (e.g., [7], [21], [22]) use the pixel information directly to maximize a measure of similarity between images, while feature methods (e.g., [23]–[25]) first detect interest points and match derived features. Among pixel based methods, cross-correlation algorithms are the most popular and they have been used for a long time for motion estimation from SAR [6]. Using drifting ice buoys as reference, studies on the accuracy of CC methods with SAR have reported root mean squared error (RMSE) values as low as 300 m when using buoy data [22]. Hollands and Dierking [26] obtained RMSE values in the order of 400-560 m using manually drawn vectors as a reference. For comparison, a feature matching method was recently presented with a reported RMSE of 202 meters when compared to manually drawn vectors [25]. However, the accuracy will vary depending on the time separation between the images as longer time separation increases the chance of image pattern decorrelation. Thus, it is expected that studies combining multiple satellites like Sentinel-1 A and B will perform well just due to the increased time resolution. The specific algorithm used in our example is as follows.

Given two detected images A_1 and A_2 and a set of latitude/longitude positions $(\theta_{lat}(k), \theta_{lon}(k)), k = 1, \ldots, K$, we find the pixel corresponding to the geographical reference point in each of the two images, $\boldsymbol{p}_1(k) = (x_1(k), y_1(k))$ and $\boldsymbol{p}_2(k) = (x_2(k), y_2(k))$. Around each point we extract a square block of data with side length $w = 129$ (~ 6.5 km) and compute the normalized cross-correlation (NCC)

$$\rho(s_x, s_y) = \sum_x \sum_y b_1(x, y) b_2(x + s_x, y + s_y) \qquad (20)$$

where the image blocks b_1 and b_2 have been normalized by subtracting the mean and dividing by the standard deviation. The offset that maximizes the correlation is taken as an estimate of the displacement of the reference point in pixels

$$\hat{\boldsymbol{s}} = (\hat{s}_x, \hat{s}_y) = \arg\max_{(s_x, s_y)} \rho(s_x, s_y) \qquad (21)$$

where coordinates are relative to the block center. Thus, if we extract a block from A_2 centered on $\boldsymbol{p}_2' = \boldsymbol{p}_2 + \hat{\boldsymbol{s}}$ it should look similar to b_1. Blockwise correlation is repeated independently for each geographical refrence point, forming a collection of point correspondences $\{(\boldsymbol{p}_1(k), \boldsymbol{p}_2'(k))\}_{k=1}^{K}$.

The algorithm blindly maximizes the correlation which may be low over e.g. open ocean. Therefore, some of the estimated vectors will likely be incorrect. It is common to reduce incorrect vectors by thresholding the NCC under the assumption that low NCC values indicate incorrect matches. In our case all vectors with an NCC value of less than 0.3 were discarded. However, this is often not enough to filter out all incorrect matches. Therefore, several algorithms employ a two-pass strategy where the first pass matches reference points from A_1 to A_2 and the second pass takes the matched points

$\boldsymbol{p}_2'(k)$ as reference points in A_2 searching for matches $\boldsymbol{p}_1''(k)$ in A_1 [7], [21]. If the estimate obtained in the backward pass agrees with the initial reference point ($||\boldsymbol{p}_1(k) - \boldsymbol{p}_1''(k)|| = 0$) the match is accepted. This strategy removed the majority of the incorrect points.

Several motion estimation algorithms include steps to account for large displacements using multi-resolution analysis [27] and some also include rotation estimation via the log-polar transform [7], [28]. The short time lag between the scenes used in this work made such optimizations not necessary and we settled for a very basic implementation.

SAR images are degraded by speckle, a noise-like phenomenon which is a consequence of the coherent imaging process [29]. Speckle is often modeled as multiplicative noise which means that high intensity areas have a larger intensity variation than low backscatter areas. Better estimates of the noise free backscatter intensities can be obtained through a process known as *multilooking*, where the SAR signal bandwidth is split into a set of frequency bands. An image ("*look*") is formed from each band, and all looks are incoherently averaged to form a smoothed (lower resolution) version of the original image. Typically, wide swath SAR data are already multilooked when delivered (see table I), so no further smoothing has been applied. Before input to the correlation algorithm, the following preprocessing was applied using the open source Sentinel-1 Toolbox [30]. A logarithmic transformation of the image intensities was used to reduce the dynamic range of the data and ease visual interpretation. Each image was then geocoded to a North Polar Stereographic projection using square pixels with a spacing of 40 m (the nominal pixel spacing for S1A) including terrain correction with a high resolution digital elevation model (DEM) for Svalbard.

V. RESULTS AND DISCUSSION

To assess that the CC algorithm performs as expected we compared the estimated CC drift with GPS positions of the research vessel Lance which was frozen into and drifting with the ice. We placed a reference point at the GPS coordinate that was closest in time to scene S1 and measured the drift between S1 and R1 for that specific position. The estimated displacement differed from the GPS position by less than one pixel in the geocoded image (within 40 m). The accuracy is attributed to the small time lag between S1 and R1 and will in general be poorer. Depending on the amount of deformation and speckle, the matching could in general be off by several pixels. Using 100 m pixels and longer time lags between images, earlier validation studies found RMSE values of around 400–600 m for similar correlation algorithms [7], [27]. The geolocation accuracy of S1A over land has been found to be very good [31]. However, the combined effects of speckle, changing viewing geometry (ascending and descending pass from different satellites), interpolation artifacts and geolocation uncertainty over ocean means that sub-pixel displacement estimation will likely not make sense. Therefore, no sub-pixel estimation was implemented, which optimistically limits the resolvable displacements to the pixel spacing of the geocoded
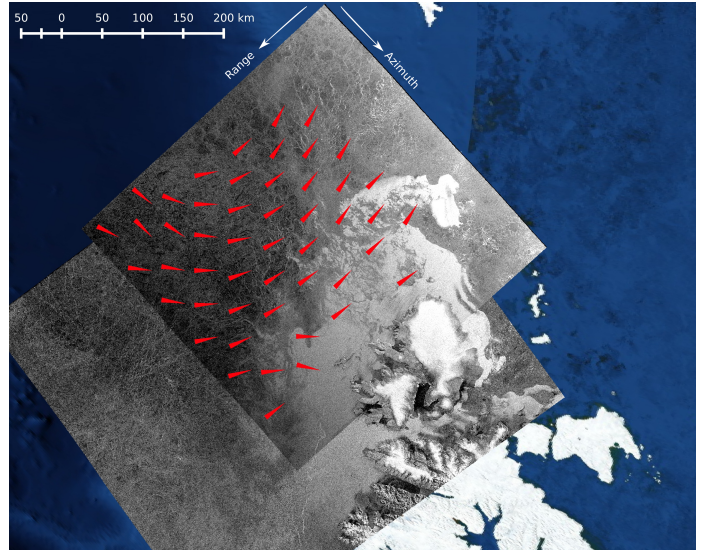

Figure 2: Amplitude SAR images in a polar stereographic projection with overlaid displacement vectors showing ice moving from West to East. Only a subset of the estimated vectors are shown and the length of the vectors has been greatly exaggerated in order to indicate the overall flow direction. The northern part of Svalbard is visible in the lower end of the images. Satellite flight and look directions are indicated by white arrows.

product. Hence, a time lag of 25 minutes and pixel size of 40 m means we cannot resolve speeds less than 3 cm/s. In order to assess the impact of speckle and the changing viewing geometry on the estimated CC drift we look at displacements estimated over land assuming that the land is stationary during the time between acquisitions. A DEM with a resolution of 50 m was used for terrain correction during geocoding and visual inspection of the coastline shows good agreement between scenes. A few one pixel displacements were found over land which is attributed to speckle and interpolation noise. This gives an estimate of the noise in the CC drift and displacements less than two pixels were therefore ignored in the comparison.

To simplify comparison between the Doppler derived drift and the correlation drift (section V-B) we used the center of each Doppler grid cell as reference positions when estimating the CC drift. This allows direct cell-to-cell comparison without further interpolation. Because of the small time lag the displacements measured using CC between S1 and R1 were also small. Therefore, visual inspection of the arrows at their true scale does not easily reveal trends in the flow. Instead, fig. 2 shows a subset of the displacement vectors where the length has been greatly exaggerated to illustrate the relative changes in flow direction across the image as ice drifts from West to East. At near to mid range, the flow is almost directly towards the LOS of the antenna which should allow good estimation of the Doppler component. At far range, however, the flow direction has a stronger along-track component (left hand side of fig. 2) than across-track and hence the observable speeds using the Doppler estimator should be lower. The pair (S1,
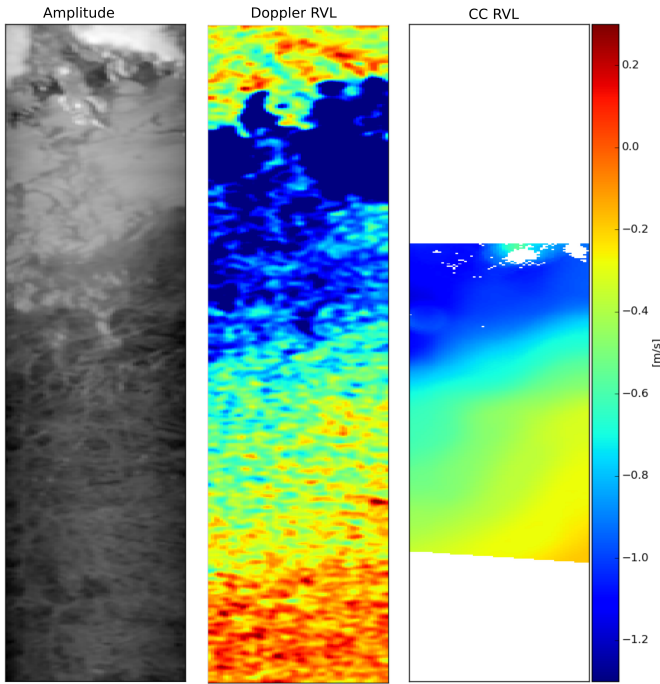
Figure 3: Side-by-side comparison of Doppler-derived speeds (middle) to CC speeds projected onto the LOS (right) for the EW3 swath. The amplitude image (left) is oriented with azimuth up and range right and shows the sea ice in the bottom half and open ocean as well as the North end of Svalbard in the upper half.

R1) was aquired during high wind conditions with mean wind speeds between 15 and 16 m/s in the time between the two scenes. Corresponding ice drift speeds as measured with the ship GPS were 0.26–0.31 m/s over the same period. Because of the gradients in the drift direction and the high drift speeds caused by the wind, the pair (S1, R1) represents the ideal case for a direct comparison between the Doppler derived drift and the CC drift. The rationale is that if it is not possible to observe the drift under these conditions, there is little hope in measuring slower drift speeds (which is the normal situation [32]).

Before comparing the cross-correlation and radial surface velocity measurements it is worth considering sources of uncertainty to allow correct interpretation of the results.

A. Doppler calibration

The two main challenges for estimating sea ice drift using Doppler shifts is estimator variance and mispointing detemination. For Sentinel-1A, an offset of 1 Hz in Doppler would translate to an error in the line-of-sight velocity of 2.8 cm/s. When the incidence angle is taken into account in the conversion to ground range, the 1 Hz error grows to 3.8 cm/s at 47° and 8.6 cm/s at 19°. Average ice drift speeds in the central Arctic are in the order of 3–20 cm/s [32]. Thus, accumulated errors of a few Hz quickly reaches the target speeds we want to measure and it is therefore imperative that all known system effects are taken into account before interpretation of the Doppler anomaly measurements. The precision of the

Doppler estimator is good with standard deviations in in the order of 2–5 Hz over homogeneous rain forest areas for EW model data with an estimation cell size of roughly 6 km × 6 km. Assuming bias-free correction of the mispointing and geometric Doppler, further reduction of the standard deviation should be possible using ensemble averaging.

Figure 4 shows examples of mispointing profiles estimated from rainforest data (scenes S2 and S3) and profiles predicted by the antenna model from [13] for each of the S1A EW swaths. For the HH polarization, the electronic mispointing profiles predicted by the S1A antenna model coefficients provided by Airbus Defence and Space do not agree well with Doppler profiles estimated from rainforest data for all swaths. The profiles for EW1 and EW2 deviate significantly in shape from profiles estimated from data and hence it is difficult to draw any conclusion from these swaths. For EW3–EW5, the deviation between model and data is generally less than the variability of the Doppler estimator. The agreement between the antenna model and estimates from data seems to be better in the case of vertical polarization, although EW1 and EW2 still have significant deviations. It would therefore be interesting to perform this analysis using vertical transmit/vertical receive (VV) data as opposed to HH. Unfortunately, no S1A VV polarization data were over ice during the N-ICE campaign.

Assuming that electronic mispointing profiles are accurate the mispointing profiles can be joined to form a single profile covering all swaths. Any residual offset can then be accounted for by subtracting the average Doppler offset calculated over flat and homogeneous land areas. However, given that our knowledge of the mispointing is poor for some swaths we have chosen to calibrate each swath individually by subtracting the mispointing profile and subsequently removing any residual offset over land. This prevents any errors in mispointing from EW1 and EW2 to propagate into the other swaths. Note that EW5 does not cover any land areas and therefore only the mispointing profile has been accounted for in this swath.

The S1A satellite uses total zero-Doppler steering to provide a nominally zero geometric Doppler. However, [33] presented data-derived geometric Doppler estimates using S1A wave mode data over land which revealed a latitude-dependent geometric Doppler variation with offsets up to 50 Hz. Geometric Doppler values as predicted using the downlinked quaternions are severely underestimated.

B. Comparing Doppler derived velocities and cross-correlation velocities

The calibrated Doppler RVL product can now be compared to the drift measured using CC. For direct comparison, the CC velocities were projected onto the ground projection of the vector pointing from the sensor to the center of the Doppler estimation cell. Since the CC drift used reference points placed at the cell centers, no interpolation of the vectors was required. A side-by-side comparison between (i) CC drift as measured between S1 and R1, projected onto the LOS of S1 and (ii) Doppler derived speeds obtained using only S1 is shown in fig. 3. The ice edge is easily identified as an abrupt transition

SENTINEL-1A EW HH 2015-12-27T10:03:58   SENTINEL-1A EW VV 2016-01-15T09:55:46
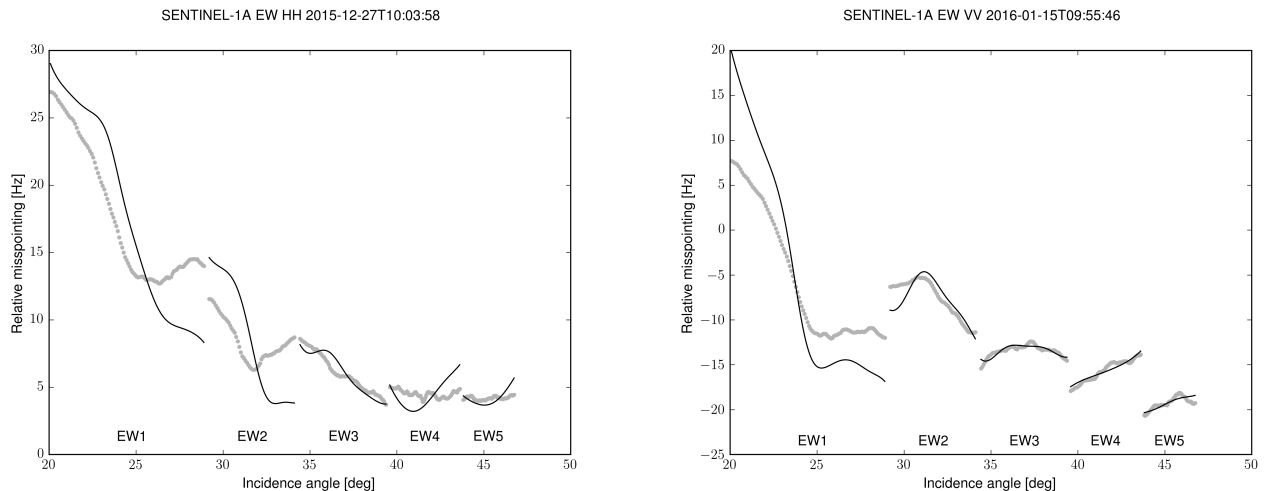
Figure 4: Comparison between electronic mispointing estimated from data and predicted by antenna model showing much better agreement for VV than HH. Gray dots indicate estimates from data while the solid black line shows antenna model predictions.

from lower to higher speeds and the overall gradient in the drift speeds is also similar in the two RVL plots. Figure 5 shows binned scatter plots between these two measurements for each of the EW swaths.

As explained above, EW1 and EW2 have larger uncertainties with respect to mispointing and geometry correction. These two swaths also contain a large amount of wide open cracks in the ice which is likely to bias the Doppler estimates. We are therefore not able to interpret the results with much confidence, however, they are shown for completeness. Furthermore, $1/\sin(\theta_i)$ changes dramatically from near range (EW1) to far range (EW5), causing errors at near range to scale very quickly when converted to ground range (see eq. (6)). Hence, we expect the variance of the ground projected Doppler estimates to improve as we go from near towards far range.

Except in the marginal ice zone (MIZ), leads in EW3–EW5 seem to be small. We therefore expect the signal away from the MIZ to be predomenantly from the ice. Linear regression between the two variables gives a slope around 1.3 which indicates that calibration of the Doppler is not perfect. This is not surprising as we do not have perfect knowledge of the antenna mispointing as well as a known underestimation of the geometric Doppler contribution as mentioned earlier. Drift speeds above 0.5 m/s are all observed in the MIZ and open water. We were able to obtain CC drift in these areas because of floating bands of ice in the open water that could be matched reliably. It is clear that the Doppler signal in the MIZ and open water is dominated by waves and ripples on the water surface. Hence, the two methods no longer measure the same thing and the CC values therefore underestimate the "drift" due to the wind. The CC drift speeds saturate around 1 m/s which is high, but not unheard of during storms.

Due to the size of the estimator variance relative to the expected ice drift speeds it is likely not meaningful to interpret the Doppler values on a pixel-by-pixel basis. Over open ocean, the observed Doppler will be a combination of contributions from swells, surface wind and surface currents. Dense pack ice far away from the MIZ should in principle be the easiest to interpret under the assuption that vertical motion can be neglected. In general however, the assumption of no vertical motion component in the ice may not be valid until several kilometers into the MIZ [34]. However, if leads are present within a resolution cell there will unavoidably be a mix between signals from ice and water. This is even more complicated in the MIZ where we always have a mix of ice and water. Also, ridges, rubble fields, brash ice or frost flowers cause intensity variations relative to smooth ice. Fourier based Doppler estimators are very sensitive to such intensity variations and it has been shown that the uncertainty of the Doppler estimates grows as the within-cell contrast grows [19]. Large intensity contributions from the side-bands are accounted for during Doppler estimation, but the within-cell variance is still an open issue. Madsen [18] proposed a Doppler estimator that only considered the signs of the real and imaginary part of the SLC data to make the estimator more robust to intensity variations, however it did not account for the side-bands.

The Doppler method struggles to reliably estimate the speed of slow moving ice. The advantage of the Doppler method lies in its ability to obtain estimates even when the assumption of pattern stability does not hold. This becomes especially relevant when the ice is fast moving and we therefore consider the Doppler method to be complimentary to CC drift estimation. However, if the reason for lack of pattern stability is that the surface has gone from dry to wet, the loss of backscatter and hence low SNR means that the Doppler shift cannot be measured reliably. Mixing of signals from ice and water could potentially be solved by separate Doppler estimation over ice and water. However, automated ice/water discrimination using SAR data is not trivial and estimation of the Doppler centroid over irregular regions needs to be further explored.

For the Doppler-derived measurements, significant spatial
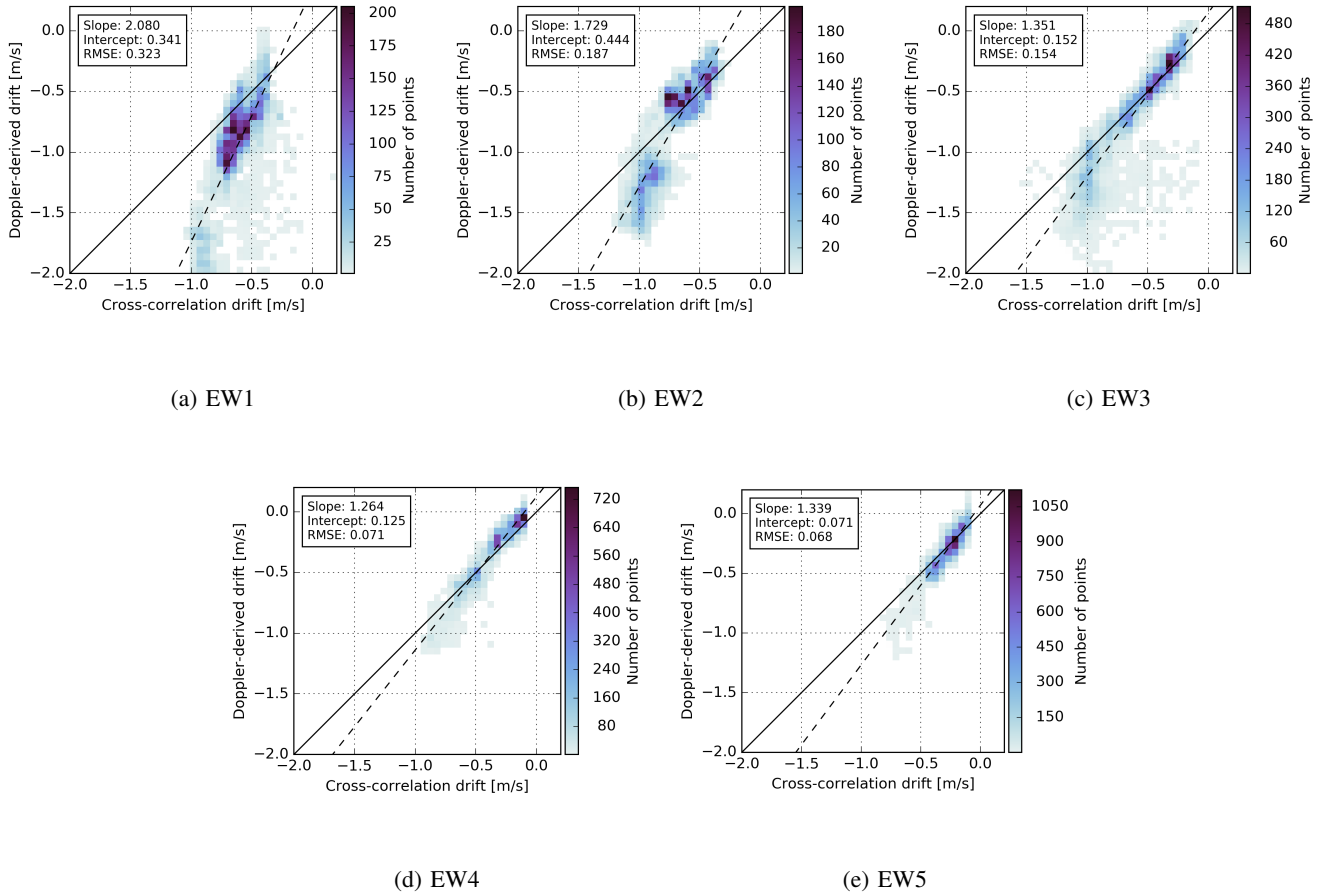
(a) EW1

(b) EW2

(c) EW3

(d) EW4

(e) EW5

Figure 5: Scatter plot between projection of CC vectors onto LOS of scene S1 (x-axis) and Doppler radial surface velocities (y-axis). The solid line is the one-to-one line and the dashed line shows a least squares linear regression between the two variables with parameters listed in the box. The drift from West to East (see fig. 2) means that the drift is towards the radar and hence we get negative speeds.

averaging was needed to reduce the variance. Before creating the scatter plot the Doppler measurements were averaged over a region of 11 x 11 km. The flow field measured between S1 and R1 was highly regular with smooth large scale trends as shown in fig. 2. However, in general there may be fronts and shear zones introducing discontinuities in the Doppler grid in which case averaging over such a large area may not be meaningful. The combination of low spatial resolution and the necessity of spatial averaging over large geographical areas to reduce estimator variance means that the EW mode is not ideal for large scale investigations of Doppler derived ice speeds. Higher resolution modes like the interferometric wide swath (IW) or wave modes implemented on S1A are likely better candidates for panarctic studies.

VI. Conclusion

We have presented SAR Doppler measurements for sea ice motion estimation using the preferred modes for operational monitoring of Arctic sea ice; ScanSAR Wide for Radarsat-2 and EW for Sentinel-1A. For fast moving ice we are able to see a trend in the Doppler derived velocities which is consistent with velocities observed using cross-correlation. Calibration of the Doppler offsets is difficult because it requires accurate knowledge of the antenna in addition to a land reference for absolute calibration. Furthermore, estimation of low drift speeds requires substantial spatial averaging to reduce estimation uncertainty. The smoothing must also make sense over the relevant geophysical scales, i.e., we want to avoid averaging over local deformation zones. With average drift speeds in the Arctic in the order of 3–20 cm/s [32], the EW mode will not be able to obtain Doppler estimates with the required precision for the majority of cases. More precise measurements can likely be obtained by using the higher-resolution modes like IW or wave mode data instead of the EW mode. As our knowledge of the electronic mispointing of the antenna improves and restituted attitude data becomes available, the proposed methodology could potentially be used (in combination with buoy measurements) for calibration of Doppler-derived radial surface velocities even without land as reference.

APPENDIX A
MERGING BURSTS INTO A CONTINUOUS SWATH

Targets located at the start and end of a burst have not been illuminated by the entire antenna pattern and hence only a partial azimuth spectrum can be obtained in these regions. However, the TOPS mode sweeping is designed such that there is a slight overlap in azimuth between successive bursts within a given swath. The simplest merging strategy would be to truncate the start and end of each burst so that there is no overlap between neighboring bursts and position them at the correct azimuth offset in the merged grid. In principle the bursts could just be cut at the center of the overlap and glued together, but in order to preserve the spectral shape in the overlap we use a slightly more involved approach.

Given a set of deramped full-bandwidth SLC bursts, $I_d^{(m)}(t)$ we first defocus the data using

$$I_{df}^{(m)}(t) = I_d^{(m)}(t) * c^*(\tau) \tag{22}$$

where c^* is the conjugate of the chirp used for azimuth compression. We then apply a window w_b in the azimuth direction

$$I_w^{(m)}(t) = I_{df}^{(m)}(t) w_b(t, \tau - \tau_c^{(m)}) . \tag{23}$$

which tapers the partially exposed data at the burst edges. The window is constructed such that the power contributions from two overlapping bursts at any given azimuth time sum to one:

$$\sum_m w_b^2(t, \tau - \tau_c^{(m)}) = 1.$$

We then refocus the data in azimuth, which makes the window above a sliding window in the azimuth time–frequency diagram:

$$I_{rf}^{(m)}(t) = I_w^{(m)}(t) * c(\tau) \tag{24}$$

The requirement that the total power contribution of all overlapping bursts sum to one at any azimuth time means that we can produce a merged image by summing the contributions on a common grid:

$$I(t) = \sum_m I_{rf}^{(m)}(t). \tag{25}$$

Note that the above procedure assumes that all bursts are focused onto the same grid, i.e. every line falls at an integer multiple of the sample spacing relative to the start time of the merged data grid. Otherwise, the data has to be interpolated onto the common grid before the final summation.

REFERENCES

[1] M. Aulard-Macler, "Sentinel-1 Product Definition S1-RS-MDA-52-7440," MacDonald, Dettwiler and Associates Ltd., Tech. Rep., 2011, p. 129.

[2] B. Chapron, F. Collard, and F. Ardhuin, "Direct measurements of ocean surface velocity from space: Interpretation and validation," *Journal of Geophysical Research*, vol. 110, no. C7, pp. 1–17, 2005.

[3] M. W. Hansen, K. Kloster, K.-F. Dagestad, S. Sandven, and J. A. Johannesen, "Retrieval of sea ice drift from SAR Doppler shift," in *Proc. ESA Living Planet Symposium (SP-709)*, Bergen: ESA, 2010, p. 5.

[4] T. Kræmer, H. Johnsen, and C. Brekke, "Emulating Sentinel-1 Doppler Radial Ice Drift Measurements Using Envisat ASAR Data," *IEEE Transactions on Geoscience and Remote Sensing*, vol. 53, no. 12, pp. 6407–6418, 2015.

[5] T. Kræmer, C. Brekke, and H. Johnsen, "Improving Doppler frequency estimation from Envisat data," in *IEEE Geoscience and Remote Sensing Symposium*, IEEE, 2014, pp. 1124–1127.

[6] M. Fily and D. A. Rothrock, "Sea ice tracking by nested correlations," *IEEE Transactions on Geoscience and Remote Sensing*, vol. GE-25, no. 5, pp. 570–580, 1987.

[7] A. S. Komarov and D. G. Barber, "Sea Ice Motion Tracking From Sequential Dual-Polarization RADARSAT-2 Images," *IEEE Transactions on Geoscience and Remote Sensing*, vol. 52, no. 1, pp. 121–136, 2014.

[8] M. Granskog, P. Assmy, S. Gerland, G. Spreen, H. Steen, and L. Smedsrud, "Arctic Research on Thin Ice: Consequences of Arctic Sea Ice Loss," *Eos*, vol. 97, 2016.

[9] *RADARSAT-2 Product Description RN-SP-52-1238, Issue 1/6*, 2009.

[10] I. G. Cumming and F. H. Wong, *Digital processing of synthetic aperture radar data: algorithms and implementations*. Artech House, 2005, p. 625.

[11] A. Recchia, A. Monti Guarnieri, N. Miranda, F. Collard, D. D'Aria, and D. Giudici, "Impact of the antenna stability on the Doppler Centroid frequency," in *Proc. IGARSS*, IEEE, 2011, pp. 1516–1519.

[12] H. Fiedler, E. Boerner, J. Mittermayer, and G. Krieger, "Total Zero Doppler Steering–A New Method for Minimizing the Doppler Centroid," *IEEE Geoscience and Remote Sensing Letters*, vol. 2, no. 2, pp. 141–145, 2005.

[13] M. Bachmann, M. Schwerdt, and B. Bräutigam, "Accurate Antenna Pattern Modeling for Phased Array Antennas in SAR Applications–Demonstration on TerraSAR-X," *International Journal of Antennas and Propagation*, vol. 2009, pp. 1–9, 2009.

[14] M. Bourbigot, "Sentinel-1 IPF Auxiliary Product Specification (S1-RS-MDA-52-7443)," European Space Agency, Tech. Rep., 2015.

[15] G. Engen and Y. Larsen, "Efficient Full Aperture Processing of TOPS Mode Data Using the Moving Band Chirp Z-Transform," *IEEE Transactions on Geoscience and Remote Sensing*, vol. 49, no. 10, pp. 3688–3693, 2011.

[16] F. De Zan and A. Monti Guarnieri, "TOPSAR: Terrain Observation by Progressive Scans," *IEEE Transactions on Geoscience and Remote Sensing*, vol. 44, no. 9, pp. 2352–2360, 2006.

[17] G. Franceschetti and R. Lanari, *Synthetic Aperture Radar Processing*, 1st ed. CRC Press, 1999.

[18] S. N. Madsen, "Estimating the Doppler centroid of SAR data," *IEEE Transactions on Aerospace and Electronic Systems*, vol. AES-25, no. 2, pp. 134–140, 1989.

[19] R. Bamler, "Doppler Frequency Estimation and the Cramér-Rao Bound," *IEEE Transactions on Geoscience and Remote Sensing*, vol. 29, no. 3, pp. 385–390, 1991.

[20] G. Engen and H. Johnsen, "High-precision Doppler frequency estimation for ocean applications," in *Proc. SEASAR (SP-709)*, Tromsø: ESA, 2012, pp. 1–4.

[21] T. Hollands, S. Linow, and W. Dierking, "Reliability Measures for Sea Ice Motion Retrieval From Synthetic Aperture Radar Images," *IEEE Journal of Selected Topics in Applied Earth Observations and Remote Sensing*, vol. 8, no. 1, pp. 67–75, 2014.

[22] A. Korosov and P. Rampal, "A Combination of Feature Tracking and Pattern Matching with Optimal Parametrization for Sea Ice Drift Retrieval from SAR Data," *Remote Sensing*, vol. 9, no. 3, p. 258, 2017.

[23] J. Daida, R. Samadani, and J. F. Vesecky, "Object-oriented feature-tracking algorithms for SAR images of the marginal ice zone," *IEEE Transactions on Geoscience and Remote Sensing*, vol. 28, no. 4, pp. 573–589, 1990.

[24] S. Muckenhuber, A. A. Korosov, and S. Sandven, "Open-source feature-tracking algorithm for sea ice drift retrieval from Sentinel-1 SAR imagery," *Cryosphere*, vol. 10, no. 2, pp. 913–925, 2016.

[25] D. Demchev, V. Volkov, E. Kazakov, P. F. Alcantarilla, S. Sandven, and V. Khmeleva, "Sea Ice Drift Tracking From Sequential SAR Images Using Accelerated-KAZE Features," *IEEE Transactions on Geoscience and Remote Sensing*, vol. 55, no. 9, pp. 5174–5184, 2017.

[26] T. Hollands and W. Dierking, "Performance of a multiscale correlation algorithm for the estimation of sea-ice drift from SAR images: initial results," *Annals of Glaciology*, vol. 52, no. 57, pp. 311–317, 2011.

[27] M. V. Thomas, C. Kambhamettu, and C. A. Geiger, "Motion tracking of discontinuous sea ice," *IEEE Transactions on Geoscience and Remote Sensing*, vol. 49, no. 12, pp. 5064–5079, 2011.

[28] A. Berg and L. E. B. Eriksson, "Investigation of a Hybrid Algorithm for Sea Ice Drift Measurements Using Synthetic Aperture Radar Images," *IEEE Transactions on Geoscience and Remote Sensing*, pp. 1–11, 2013.

[29] C. Oliver and S. Quegan, *Understanding Synthetic Aperture Radar Images*. Artech House, 1998, vol. 42, p. 479.

[30] *SNAP - ESA Sentinel Application Platform software v3.0.4, http://step.esa.int*, 2016.

[31] A. Schubert, D. Small, N. Miranda, D. Geudtner, and E. Meier, "Sentinel-1A Product Geolocation Accuracy: Commissioning Phase Results," *Remote Sensing*, vol. 7, pp. 9431–9449, 2015.

[32] M. H. Halvorsen, L. H. Smedsrud, R. Zhang, and K. Kloster, "Fram Strait spring ice export and September Arctic sea ice," *The Cryosphere Discussions*, vol. 9, no. 4, pp. 4205–4235, 2015.

[33] H. Johnsen, V. Nilsen, G. Engen, A. A. Mouche, and F. Collard, "Ocean doppler anomaly and ocean surface current from Sentinel 1 TOPS mode," in *Proc. IGARSS*, IEEE, 2016, pp. 3993–3996.

[34] F. Ardhuin, J. Stopa, B. Chapron, F. Collard, M. Smith, J. Thomson, M. Doble, B. Blomquist, O. Persson, C. O. Collins, and P. Wadhams, "Measuring ocean waves in sea ice using SAR imagery: A quasi-deterministic approach evaluated with Sentinel-1 and in situ data," *Remote Sensing of Environment*, vol. 189, no. January, pp. 211–222, 2017.